JGR Space Physics

RESEARCH ARTICLE
10.1029/2019JA026576

Formation of the Potential Jump Over the Geomagnetically Quiet Sunlit Polar Cap Region

G. V. Khazanov[1], E. N. Krivorutsky[1], and D. G. Sibeck[1]

[1]NASA Goddard Space Flight Center, Greenbelt, MD, USA

Key Points:
- Formation of field-aligned electrostatic potential drops in the sunlit polar cap during geomagnetically quiet conditions is considered
- The role of the polar rain electrons in the formation of electrostatic potential jumps in the polar cap region is studied
- The influence of photoelectron energy distribution function on the polar cap potential drop is analyzed

Correspondence to:
G. V. Khazanov,
george.v.khazanov@nasa.gov

Citation:
Khazanov, G. V., Krivorutsky, E. N., & Sibeck, D. G. (2019). Formation of the potential jump over the geomagnetically quiet sunlit polar cap region. *Journal of Geophysical Research: Space Physics*, *124*, 4384–4401. https://doi.org/10.1029/2019JA026576

Received 30 JAN 2019
Accepted 16 MAY 2019
Accepted article online 24 MAY 2019
Published online 27 JUN 2019

Abstract We consider the formation of a potential drop over the Earth's polar cap during geomagnetically quiet daytime. The observed potential drop is primarily defined by the hydrogen, photoelectron, and polar rain fluxes ratios and depends strongly on the energy distribution of the photoelectron flux. Polar rain is an essential component of the model required for plasma quasi-neutrality. The potential distribution along the magnetic field line has two regions, with a small, gradual, potential drop of 3–4 V and a potential jump. The value of the potential jump depends on the hydrogen ion to photoelectron flux ratio and is also controlled by polar rain electrons. With quasi-neutrality required at its upper boundary, the jump only occurs in the presence of polar rain and its location depends on the polar rain flux. Model predictions compare well with FAST observations presented by Kitamura et al. (2012, https://doi.org/10.1029/2011JA017459).

1. Introduction

Plasma outflow is a general phenomenon observed at many solar system bodies. Heavy ion outflow during disturbed magnetospheric conditions affects the dynamics of the magnetosphere and leads to a number of consequences: the ions can reduce the cross-cap potential, influence dayside reconnection, and alter the behavior of the plasma sheet, etc. (e.g., Brambles et al., 2011; Wiltberger et al., 2010; Winglee et al., 2002).

Photoelectron escape from the polar cap into the magnetosphere is a part of this problem. The polar cap is a region with open magnetic field lines along which plasma can easily escape into space if plasma ions, including H^+ and O^+, with initial ionospheric energies of 0.05–0.2 eV, can overcome the gravitational barrier. Ionospheric thermal electrons have energies comparable to those of the ions, 0.1–0.6 eV, but much higher mobility. In their efforts to escape from the ions, they create polarization electric fields that help the ions to move faster and preserve quasi-neutrality. Ionospheric photoelectrons produced by solar extreme ultraviolet and X radiation interacting with neutral gases in the upper ionosphere initially have much higher mean energies, 15–25 eV. They can contribute to the formation of an additional polarization E field (Axford, 1968; Lemaire & Scherer, 1972) that further accelerates escaping polar cap ions. The day-night asymmetry of the polar wind observed by Akebono satellite at altitudes of 5,000–9,000 km (Abe et al., 1993; Yau et al., 1995) led to the conclusion that photoelectrons play an important role in the formation of ion outflows (Khazanov et al., 1997; Tam et al., 1995). Lemaire et al. (2007) and Schunk and Nagy (2009) present reviews of theoretical and observational studies of polar wind outflows.

A number of researchers have confirmed the role of photoelectrons in the formation of upward directed electric fields. DE-2 observations of downward flowing photoelectrons with energies up to 60 eV seen in the polar cap at altitudes below 1,000 km (Horwitz et al., 1992; Pollock et al., 1991; Winningham & Gurgiolo, 1982) have been interpreted as experimental evidence for such an electric field. Observations of high-speed ion beams seen on dayside polar cap field lines at high altitudes by DE-1 (Horwitz et al., 1992; Pollock et al., 1991) were also connected to escaping photoelectrons. However, the relationship between the ion beams and the photoelectrons was not conclusively established.

Kitamura et al. (2012), hereinafter referred to as KM2012, presented Fast Auroral SnapshoT (FAST) observations of photoelectron flows in the polar wind on open field lines in the polar cap during geomagnetically quiet daytime conditions. They found the presence of a field-aligned potential drop larger than 10 V in this region and attributed it to the presence of photoelectrons and the imbalance between the photoelectron and H^+ ion fluxes. KM2012 provided a comprehensive analysis of the FAST observations and concluded that

their experimental results contradict photoelectron driven polar wind models by Khazanov et al. (1997), Wilson et al. (1997), and Su, Horwitz, Wilson, et al. (1998). They found that the observed potential drop is smaller by a factor of 2–3 in comparison to the modeling results by Wilson et al. (1997) and Su, Horwitz, Wilson, et al. (1998) and the net escaping electron number flux is negatively correlated with the upward electron number flux and with the magnitude of the potential drop, while the opposite is predicted by the models. They also provided an interpretation of the experimental results with the major focus on the role of ions in forming such a large polar cap potential drop. Summarizing results concerning potential drop over the quiet time dayside polar cap, Kitamura et al. (2012, 2015) suggested that "The magnitude of the field-aligned potential drop at high altitudes is likely determined mostly by the balance between the escaping photoelectron flux and the polar wind H^+ ion flux." This citation from Kitamura et al. (2017) implies complete ionospheric control of the formation of field-aligned potential drops and completely ignores the magnetospheric input to this process.

Based on the data provided by KM2012 and Kitamura et al. (2015, 2017), this paper discusses the formation of such potential drops for quiet currentless conditions over the polar cap. It addresses some of the consequences of this phenomenon on the modeling of polar wind outflows. Considered questions are the following:

- How do potential drops depend on escaping photoelectron fluxes?
- What is the distribution of the potential drop along the magnetic field line?
- How do the potential drop and its location depend on the plasma composition?
- Is the majority of the potential drop localized?
- Are ionospheric conditions the sole factor controlling the formation of the potential jump?

We will also discuss the validity of the proposed model assumptions and some implications of these results to global modeling of plasma outflow from the polar cap. The model is described in the next section, results are presented in section 3, and section 4 contains the discussion and conclusions. Details of the calculations of plasma parameters that are involved in the potential drop formation are presented in Appendix A along with a discussion of some of the important specifics that are omitted in the main part of the paper.

2. Model Description

The model used in this study is kinetic, stationary, and collisionless for all plasma components. Their distribution functions are conserved along magnetic field lines and can be expressed as functions of the magnetic moment and total energy (kinetic + potential), which are in our case integrals of motion (see Khazanov et al., 1998, for more details). It is assumed that at some altitude along the open magnetic field line exists an abrupt potential jump; the width of the jump is neglected. We assume that cold electrons, photoelectrons, and hydrogen and oxygen ions are injected at the lower boundary, while a polar rain falls on the upper boundary. The polar rain ions are not included in the formation of the polar cap potential drop because their density is lower than the polar rain electron density according to Newell et al. (2009). Figure 1 illustrates the particle fluxes included in the model. The insert shows a sketch of the potential distribution along the magnetic field line. The potential slowly drops to φ_L between the injection point (B_0) and the lower boundary of the potential jump (B^*), where it abruptly changes to φ_U. We assume that the potential remains constant above the boundary ($B < B^*$, dashed line) potential. All particles, except the photoelectrons, have Maxwellian distributions with cold electrons, hydrogen and oxygen ions, and polar rain temperatures of 0.35, 0.15, 0.15, and 100 eV, respectively. The photoelectron energy range is 0.35–60 eV. The distribution above 4 eV was taken from KM2012 (their Figure 2c, FAST observations); for the energies below ~ 4 eV (not available from KM2012) we used theoretical fluxes presented by Su, Horwitz, Wilson, et al. (1998). All particle distributions are assumed to be isotropic at their injection altitudes.

The injection point for the photoelectrons is set at an altitude of 1,000 km (after mapping the FAST measured photoelectron distribution function from an altitude of 3,800 km). The polar rain is injected at the upper boundary of the simulation domain. This boundary is an unknown variable calculated by the model. For the thermal electrons and ions the injection point is placed at an altitude of 2,400 km. At this altitude most of the hydrogen ions are escaping ions (Lie-Svendsen & Rees, 1996). Photoelectron, hydrogen, and oxygen fluxes are prescribed at their injection points, as is the polar rain density at an altitude of 1,000 km. The density of the cold electrons is an unknown variable calculated by the model. The potential drop between

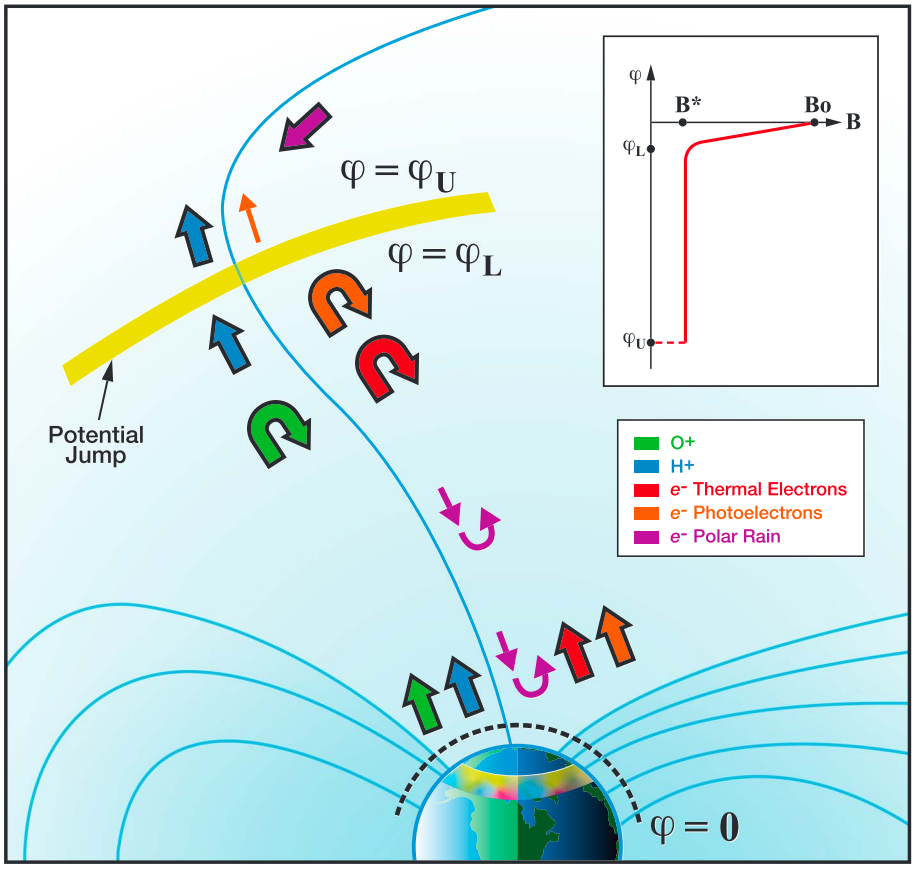

Figure 1. Qualitative representation of the potential drop formation over the dayside of the polar cap presented by the model. All notations in this figure are discussed in the paper.

altitudes of 1,000 and 2,400 km is neglected. A standard dipole magnetic field model for the polar cap with B varying as r^{-3} is used. Electric and gravitational potentials at the injection point $s = 0$ (s is the distance along the magnetic field line measured from the altitude 2,400 km) are set to 0.

It is assumed that the polarization potential, φ, satisfies two constraints (Chiu & Schulz, 1978)

$$\frac{d\varphi}{dB} > 0, \frac{d^2\varphi}{dB^2} < 0 \quad (1)$$

The same is valid for the total (polarization + gravitational) field acting on the ions with modified criteria (1) as described by Khazanov et al. (1998). It is also assumed that the particles reflected above the potential jump can be neglected. Under these restrictions the problem can be divided into two parts. First, the cold electron density at the injection point, the jump position along the field line (s^*), and the polarization potentials below (φ_L) and above (φ_U) the jump are calculated from the currentless condition and three conditions of quasi-neutrality (at the injection point and under and above the potential jump). Second, the potential distribution along the field line above $s = 0$ and below $s = s^*$ is calculated.

Particles injected at $s = 0$ can be separated into two classes: those that will be reflected between $s = 0$ and $s = s^*$ and those that escape. The latter also includes the polar rain particles reaching the lower boundary. With the conservation law along the magnetic field line, $\frac{j_\alpha^{esc}}{B} = \text{const}$, the current is defined by the balance of the escaping particle fluxes (j_α^{esc}) at any arbitrary point. The currentless condition, written at the injection point $s = 0$, is

$$\sum_\alpha e_\alpha j_\alpha^{esc}(s = 0) = 0 \quad (2)$$

where e_α is the particles charge. This equation includes escaping fluxes of photoelectrons, cold electrons, polar rain, and oxygen and hydrogen ions, specified by α. The fluxes are given by equations (A6), (A9),

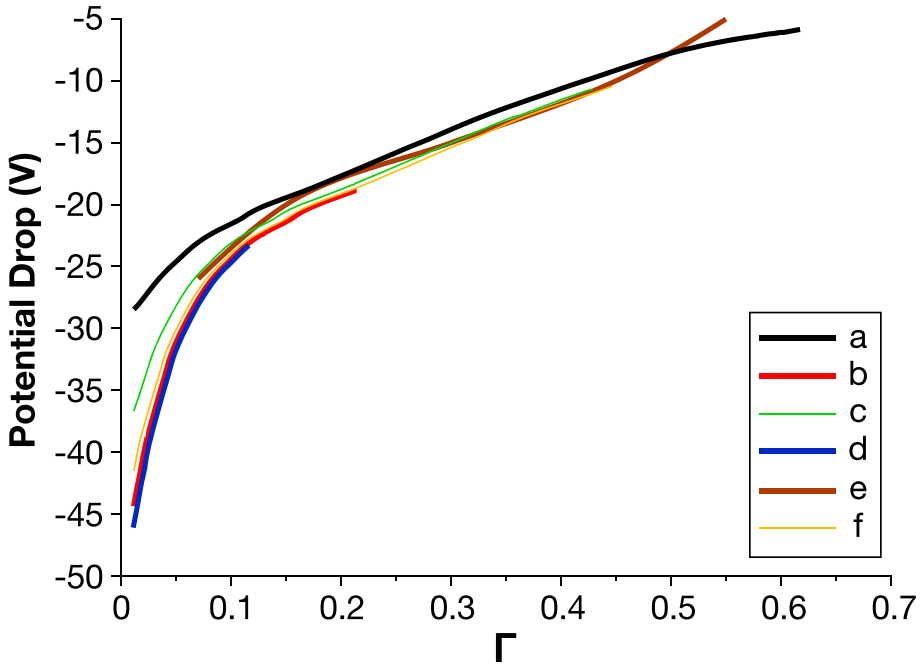

Figure 2. The total potential drop distribution as a function of photoelectron, polar rain, and ion fluxes. Here $\Gamma = j_H^{inj}/j_{ph}^{inj}$, where all fluxes are taken at $s = 0$; $n_O^{inj} = 20 n_H^{inj}$. Photoelectron and polar rain fluxes, particles number per square centimeter per second ($cm^{-2}\ s^{-1}$), are (a) $7 \cdot 10^8$ and $3.3 \cdot 10^7$; (b) $7 \cdot 10^8$ and $3.3 \cdot 10^6$; (c) $1.7 \cdot 10^9$ and $3.3 \cdot 10^7$; and (d) $1.7 \cdot 10^9$ and $3.3 \cdot 10^6$ and are presented by black, red, green, and blue lines, respectively. Brown line, e, represents the observational data by KM2012, and the yellow curve, f, corresponds to $7 \cdot 10^8$ and $6.6 \cdot 10^6$ photoelectron and polar rain fluxes.

(A11), and (A14) in Appendix A; all injected hydrogen flux is escaping and presented in (2) as a fraction of the injected flux of the photoelectrons.

Quasi-neutrality equation for the injection point $s = 0$ is given by

$$n_{ph}^{inj} + n_{ph}^{rfl} + n_{ce}^{inj} + n_{ce}^{rfl} + n_{pr}^{esc} - n_H^{inj} - n_{Ox}^{inj} - n_{Ox}^{rfl} = 0 \tag{3}$$

where "inj" and "rfl" stand for the densities of injected and reflected photoelectrons (ph), cold electrons (ce), polar rain (pr), hydrogen (H), and oxygen (Ox) ions, respectively. There is no reflected polar rain at $s = 0$, and the hydrogen ions are not reflected anywhere on the magnetic field line between $s = 0$ and $s = s^*$. The density of the reflected polar rain particles should be included in an equation similar to equation (3) below the jump at $s = s^*$

$$n_{ph}^{inj} + n_{ph}^{rfl} + n_{ce}^{inj} + n_{ce}^{rfl} + n_{pr}^{inj} + n_{pr}^{rfl} - n_H^{inj} - n_{Ox}^{inj} - n_{Ox}^{rfl} = 0 \tag{4}$$

The quasi-neutrality equation above the jump at $s = s^*$ includes the injected particles able to escape and the injected and reflected particles of the polar rain. There is also an additional population that previously was ignored in all polar wind studies, namely, trapped photoelectrons, n_{ph}^{tr}. This trapped electron population was described by Arefiev and Breizman (2009) when they considered collisionless plasma expansion into vacuum. It can be formed due to the interaction of the escaping photoelectrons with a rarefaction wave propagating above the potential jump. Such a wave is formed at the upper boundary of the jump, where the plasma density is reduced, and will propagate from the boundary in the direction of the diminishing magnetic field. Diminishing mirror force and a negligible electric field above the jump (it is assumed that above the jump the photoelectrons are not reflected) can form a maximum in the effective potential at the upper boundary, as discussed in Appendix A. Photoelectrons with energies slightly larger than this potential that overcome the maximum will be reflected by the wave, lose some energy, and will be trapped between the upper boundary of the jump and the rarefaction wave. Because we did not calculate the potential

distribution above the jump, the results related to these particles should be considered only as a rough estimation of their possible role. In this case, the quasi-neutrality equation above the jump at $s = s^*$ can be stated as

$$n_{ph}^{esc} + n_{ce}^{esc} + n_{pr}^{inj} + n_{pr}^{rfl} + n_{ph}^{tr} - n_H^{esc} - n_{Ox}^{esc} = 0 \quad (5)$$

The densities of the injected, reflected, and trapped photoelectrons needed in this equation are found from equations (A3)–(A5) as explained in Appendix A, where some additional details of the density calculations for each population are provided. The densities of other plasma components are presented by equations (A7), (A8), (A10), (A12), (A13), and (A15) as the sum of the injected and reflected particles. These four coupled equations, (2)–(5), are linear with respect to the cold electrons plasma density at the injection point. We obtained the cold electron density from equation (3), and the roots of the remaining three equations (s^*, φ_L, and φ_U) were found with the SciLab root solver with relative errors of 10^{-13}–10^{-14}. The solutions are stable, that is, independent of initial guesses about the roots.

With the known cold electron density at $s = 0$, potentials below and above the jump, and the jump position ($s = s^*$), the particle densities at arbitrary points along the magnetic field line are found from equations (A3), (A4), (A7), (A10), (A12), and (A15), and the polarization potential distribution along the magnetic field line is calculated from the local quasi-neutrality condition.

3. Model Results

3.1. Potential Jump Formation

The data presented by KM2012 were collected during 1 month, and the range of the observed photoelectron fluxes was $7 \cdot 10^8$ to $1.7 \cdot 10^9$ cm^{-2} s^{-1}. In the calculations that are presented below, we assume that electron polar rain densities at altitudes of ~1,000 km can range from 0.01 to 0.1 cm^{-3} with corresponding fluxes ranging from $3.3 \cdot 10^6$ to $3.3 \cdot 10^7$ cm^{-2} s^{-1}. The upper boundary of these fluxes is apparently larger than in the cases considered by KM2012, but their choice permits us to illustrate the role of the polar rain in the model.

KM2012 did not present or discuss polar rain fluxes. However, when referencing results shown by KM2012, Kitamura et al. (2015) presented the median polar rain flux, which is $\lesssim 3 \cdot 10^6$ cm^{-2} s^{-1}. That is why there are some uncertainties in our selection of polar rain fluxes. Gussenhoven et al. (1984), for example, found that typically the standard deviation for each spectral point of the polar rain was 50–100% of the average value. They also presented the midnight to noon gradient in the polar rain flux and the dependence of the polar rain fluxes on the interplanetary magnetic field for quiet conditions with the same *Kp* index (+2) as KM2012. The averaged fluxes vary by a factor of 2 depending on these parameters. So it can be safely assumed that the upper boundary for the polar rain fluxes during the observations presented by KM2012 is 2–2.5 times larger than their median magnitude, that is, reached densities of 0.02 to 0.025 cm^{-3}.

We found solutions to the system of equations (2)–(5) for four combinations of the photoelectron and polar rain fluxes and different hydrogen fluxes. These four combinations (a, b, c, d) are listed in the caption of Figure 2. The total potential drop along the magnetic field line is presented in this figure as a function of $\Gamma = j_H^{inj}/j_{ph}^{inj}$, where the hydrogen and photoelectron fluxes are taken at $s = 0$. As seen from the black-red and blue-green pairs of curves, for the same photoelectron fluxes an increase (decrease) in the flux of polar rain electrons leads to a potential drop decrease (increase). The polar rain electron flux in the currentless equation (2) plays the same role as the hydrogen flux; they both compensate for the current of the photoelectrons. This is also seen from Figure 2. For example, the polar rain fluxes for the red and the black curves (normalized by the injected photoelectron flux) are 0.005 and 0.05, respectively. Therefore, $\Gamma \approx 0.1$ at the red curve corresponds to $\Gamma = 0.05$ at the black curve. The polar rain flux (0.05) provides an additional current to this ion current. This leads to equal potential drops as can be seen in the figure. So the impact of the polar rain fluxes is comparable to that of the hydrogen fluxes on the potential drop for polar rain fluxes comparable with the ion fluxes. It is also seen from this plot that the polar rain electrons define the ratios of hydrogen to electron fluxes (Γ parameter domain), where solutions of the system (2)–(5) exist. As will be demonstrated below, the quasi-neutrality condition above the jump (equation (5); see discussion regarding the potential jump in section 3.2) is not satisfied without the polar rain, because of the excess of hydrogen ions.

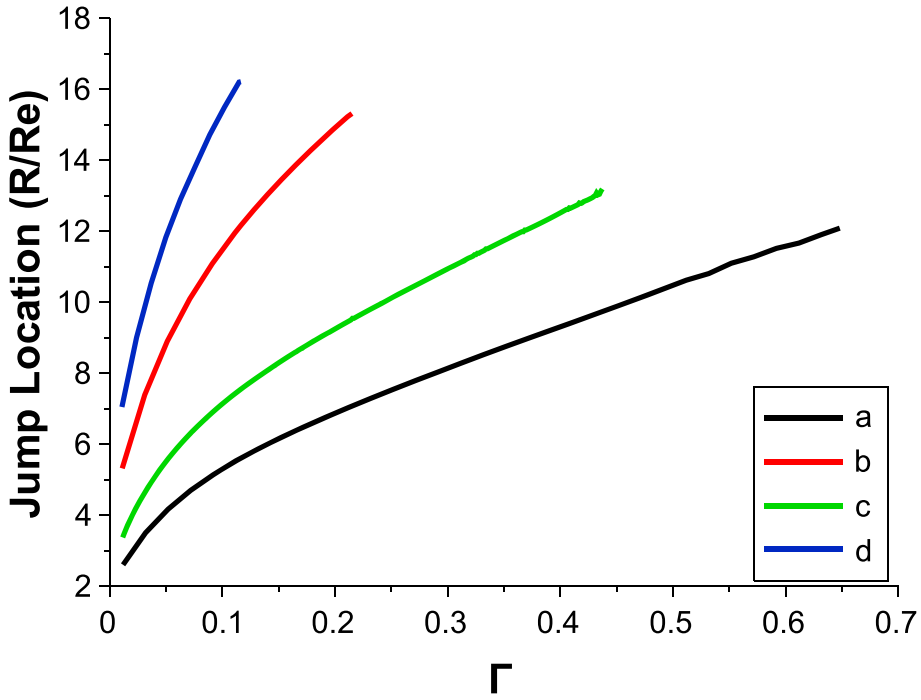

Figure 3. The potential jump location (in Earth's radii) as a function of photoelectron, polar rain, and ion fluxes. Line colors correspond to the cases presented in Figure 2 (a, b, c, and d)

Observations from KM2012 (their Figure 5) can be used to depict the dependence of the potential drop on the escaping fraction of the injected photoelectron flux; this is the brown line in Figure 2. The escaping fluxes of oxygen and cold electrons are negligible for the obtained potential drops. The parameter Γ is close to the fraction of the escaping photoelectron flux, if the polar rain fluxes are small compared to the hydrogen fluxes. In this domain of Γ the modeled potential drop is the same as observed. On the other hand, the domain of the escaping fluxes (or the domain in Γ) is not reproduced by the model for the case of weak polar rain (density 0.01 cm^{-3}, the red and blue lines) corresponding to the median polar rain found in the observations by Kitamura et al. (2012, 2015). The yellow line in the figure is calculated for polar rain densities twice the median, which is a reasonable value, as discussed above. This curve not only reproduces the magnitude of the potential jump well but also covers the main part of the observed domain of escaping photoelectron fluxes. The remaining region of $\Gamma \geq 0.47$ can be reproduced with somewhat larger polar rain fluxes. The domain in Γ, where the solutions of equations (2)–(5) exist, also depends on the currents observed during the measurements (see below), polar rain temperature, and the deviation of the polar rain distribution from Maxwellian.

The escaping fluxes of photoelectrons as well as the strength of the potential jump that forms at the upper boundary are defined primarily by the ratio between the injected hydrogen and photoelectron fluxes when hydrogen fluxes exceed polar rain fluxes. However, the solution of (2)–(5) exists only if the polar rain electrons are taken into account. The potential drop below the jump, φ_L, is in the range from 3.2 to 5.1 eV. This is comparable to the polarization potential for an oxygen and cold electron plasma in diffusive equilibrium in the Earth's gravitational field (Guglielmi et al., 1996), which is about 3 eV for the chosen injection altitude. Such a small variation of the potential below the upper boundary, s^*, clearly shows that most of the potential drop is localized and represents the potential jump in the potential drop distribution along the magnetic field line.

Figure 2 shows that the escaping fraction of the photoelectron flux (approximately equal to Γ) is negatively correlated with the magnitude of the potential drop as presented by KM2012 in their Figure 5a. The same can be seen from Figure 4 presented below.

Figure 3 presents the location of this potential jump for the same plasma parameters as in Figure 2 and demonstrates the strong dependence of its location on Γ and polar rain electrons in particular. The nature

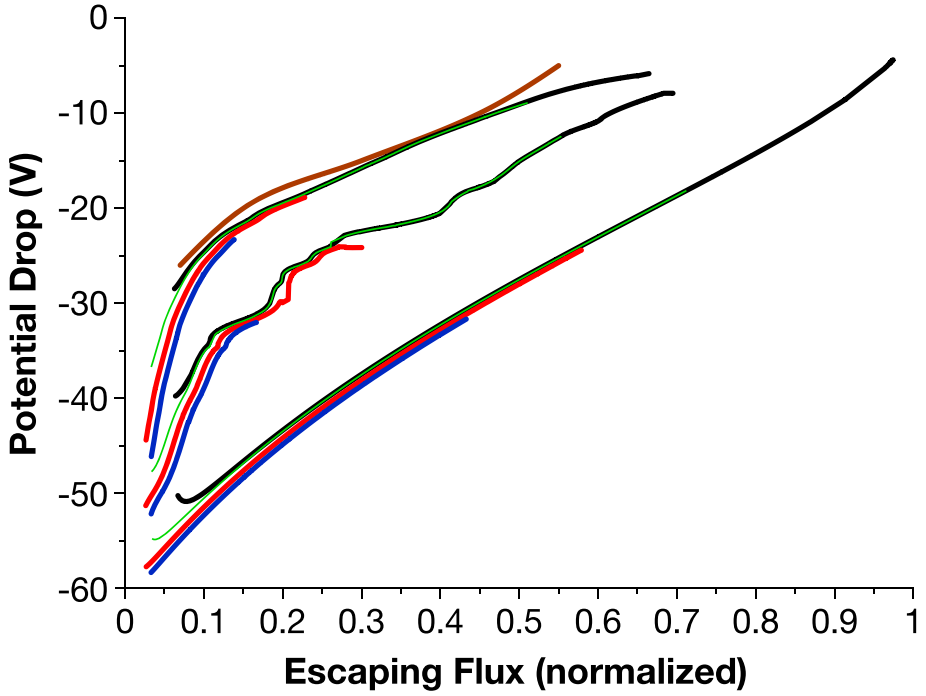

Figure 4. Potential drop-escaping photoelectron flux dependence for different photoelectron flux energy distributions. Escaping flux is normalized to the injected flux ($j_{ph}^{esc}/j_{ph}^{inj}$) at $s = 0$. In brown are the observational data. The flux structures are taken from KM2012 (upper four curves), Su, horwitz, wilson, et al. (1998; curves in the middle), and Maxwellian (lower four curves). The red and blue curves are shifted to the right at 0.01 and 0.02, respectively, in order to be distinguished. Other parameters and color coding are the same as in Figure 2.

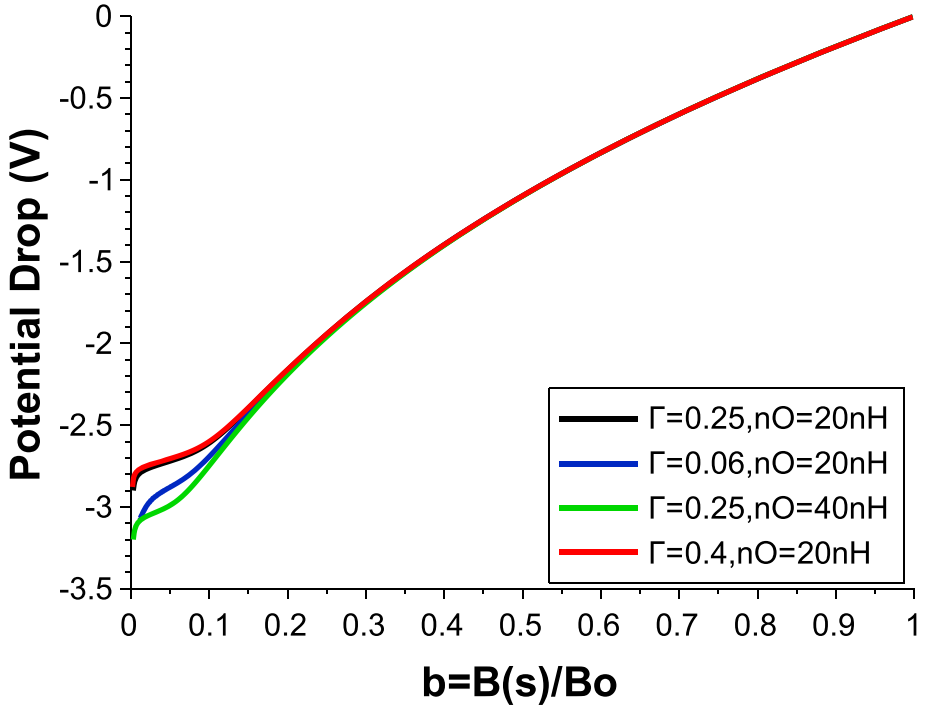

Figure 5. The potential distribution along the magnetic field line below the potential jump. Photoelectron and polar rain fluxes, particles number per square centimeter per second ($cm^{-2}\ s^{-1}$), are $1.2 \cdot 10^9$ and $1.7 \cdot 10^7$.

of the limits on Γ was discussed above. For the same Γ and photoelectron flux the potential jump location essentially changes depending on the polar rain flux, as can be seen from the black-red and blue-green pair of curves. Such a strong dependence is defined by the quasi-neutrality requirement above the jump. It should be noted that for larger distances a more accurate magnetic field description is required. The distance is directly involved only in the calculation of the gravitational potential, and the magnetic model used here remains valid throughout the distances where gravitation affects the ion motion. All other quantities are expressed by the magnetic field ratio and do not involve the magnetic field model explicitly, but this model defines the conversion of the magnetic field ratio to distance along the field line.

It should be noted that while equation (2) assumes a strictly currentless condition, the data in KM2012 were selected during a period of small field aligned currents ($\leq|0.16|\mathrm{A/m^2}$) that correspond to the electron number fluxes less than $10^8\ \mathrm{cm^{-2}\ s^{-1}}$. This current can be included in equation (2), but it only slightly affects the range of the hydrogen fluxes where the solutions of the equations (2)–(5) exist. The quasi-neutrality condition at the upper boundary of the jump is reached in the main due to the balance between the hydrogen and polar rain densities, as stated above. The input of the escaping photoelectrons to this balance is small, and the modification of the photoelectrons escaping flux that is introduced as a current does not change the situation. On the other hand, the impact of the current on the potential drop is more pronounced. For example, for average photoelectron and polar rain fluxes of $1.2 \cdot 10^9$ and $1.7 \cdot 10^7\ \mathrm{cm^{-2}\ s^{-1}}$, respectively, and $n_O^{inj} = 20 n_H^{inj}$, the change in the potential drop is about 20%.

The location of the potential jump is far enough from the injection point that the photoelectron velocity near the jump is directed approximately along the magnetic field line. Thus, the reflected portion of the photoelectrons for the prescribed potential jump is defined only by their energy distribution. Observations from KM2012 (their Figure 5) can be presented as the dependence of the potential drop on the escaping fraction of the injected photoelectron flux and is shown by the brown line in Figure 4. Three photoelectron energy distributions are considered: (a) taken from KM2012 as described above, (b) obtained from the two-stream model (Su, Horwitz, Wilson, et al., 1998) for solar maximum in 2002; and (c) a Maxwellian distribution with a temperature of 20 eV. The energy ranges and flux magnitudes of all the distributions are normalized to be the same. Consequently, only the flux energy structures are different for the three bundles of curves in Figure 4. The color of the lines corresponds to the same flux ratios as in Figure 2. The curves are continuous and overlap each other. To be distinguished, they have been shifted slightly horizontally with respect to each other.

The upper four curves are calculated for the photoelectron energy distribution taken from KM2012 (their Figure 2). The group of lines in the middle of Figure 4 is calculated using the distribution function that is obtained from the two-stream model by Su, Horwitz, Wilson, et al. (1998) and shown in this paper by their Figure 2. Compared to the photoelectron distribution measured by FAST, this photoelectron distribution function exhibits many fine-scale structures that represent variations in the solar ultraviolet and X-ray wave spectra. Such fine structures in the photoelectron spectra lead to the nonmonotonicity of the calculated total potential drops that are visible in Figure 4. Finally, the lower group of lines in this figure is calculated for Maxwellian-like photoelectron spectra as was assumed in the calculations by Wilson et al. (1997).

As can be seen from this figure, only the model results for the distribution that is taken from photoelectron data presented by KM2012 (upper four curves) agree with the observations. The potential drops that are calculated for the Maxwellian photoelectron distribution are larger and compare well to the results of Wilson et al. (1997). Hence, the potential drop required to reflect the same portion of the injected photoelectron flux strongly depends on their energy distribution function.

It should be mentioned here that the polar rain electrons have no influence on the value of potential drop needed to reflect the fixed portion of the photoelectron flux (Figure 4). The same is true for the curves that represent the different photoelectron distribution functions. However, the size of the region of the escaping fluxes where the solutions exist depends on the polar rain and differs for the three selected photoelectron distribution functions.

We also analyzed the effect of different injected oxygen fluxes (Yau et al., 2007). For oxygen densities twice as large as the cases presented in Figures 2–4 ($n_O^{inj} = 40 n_H^{inj}$), the potential drop and its position remain practically the same.

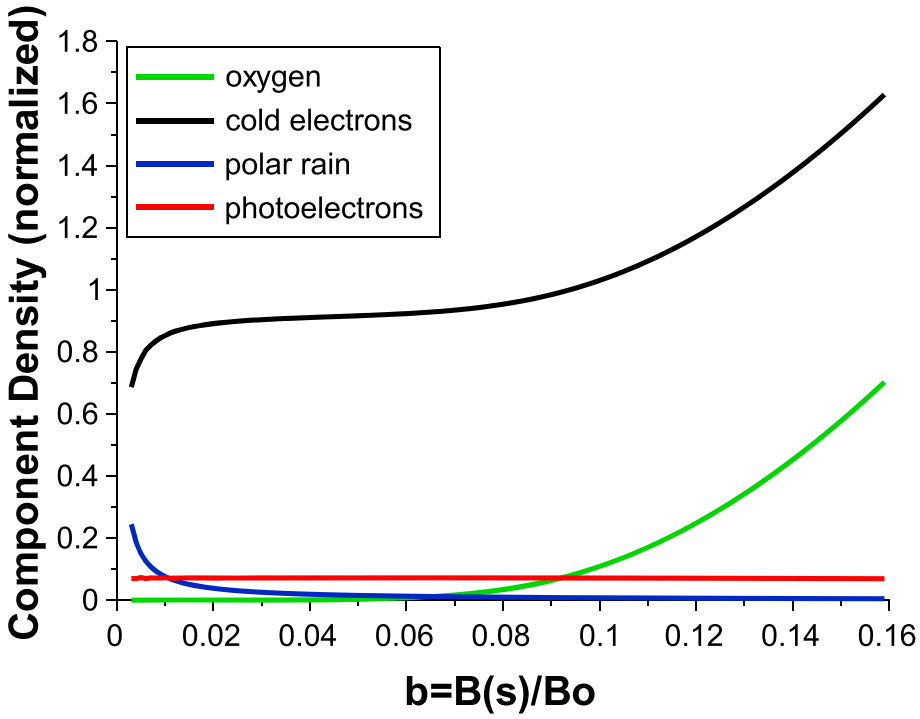

Figure 6. Normalized plasma components density distribution along the magnetic field line. The densities are normalized to the local hydrogen density. Γ = 0.25; the fluxes are the same as in Figure 5, $n_O^{inj} = 20 n_H^{inj}$.

3.2. Potential Distribution Along the Magnetic Field Line

For the known potentials above and below the jump, its position, and the density of the injected cold electrons, we calculated the potential distribution along the magnetic field line between the injection point ($s = 0$) and the lower boundary of the jump ($s = s^*$). Figure 5 presents these distributions for three magnitudes of Γ and two oxygen-to-hydrogen ion density ratios. The potential drop is independent of this ratio for large b, and it is slightly larger for larger oxygen content for small b (green and black lines). The dependence of the potential distribution on Γ is even less pronounced, and any difference can only be seen for very small Γ (=0.06, blue line) and small b. The change in the rate of the potential drop along the magnetic field line for small b is caused by the changing plasma composition with altitude. As can be seen from Figure 6 (all densities presented here are normalized to the local density of the hydrogen ions) it changes for b less than ~0.1. For large b the quasi-neutrality condition is easily supported due to the large density of cold electrons. For smaller b the total force acting on the hydrogen ions is close to 0, their motion is inertial, and their density drops because of the conserved flux and diminishing magnetic field. As can be seen from the calculations, the polar rain density in this region is close to constant. This is reflected by the behavior of the blue curve in Figure 6; for smaller b the ratio of the polar rain to the hydrogen ions densities is larger. From the black curve we see that the density of the cold electrons drops faster than the hydrogen ion density due to the polarization field acting on the electrons. The small polarization field cannot affect the density of the energetic electrons for larger s to compensate for the diminishing cold electron density and the potential jump forms at point s^*. This jump in electric potential accelerates the hydrogen ions, their density drops, and quasi-neutrality is restored at the upper boundary of the jump due to the presence of polar rain electrons. Here $n_{pr} \sim 0.95 n_H$ and $n_{ph} \sim 0.05 n_H$. The trapped photoelectrons that form between the potential jump and rarefaction wave constitute only about 40% of the photoelectrons at this position. So the quasi-neutrality condition at the upper boundary (where the potential jump forms) is reached primarily due to the balance between the polar rain and hydrogen ions densities.

It can easily be shown that the quasi-neutrality and the currentless conditions at the upper boundary of the potential jump cannot be satisfied without the polar rain. For the simplicity let us consider this using a Maxwellian distribution for the photoelectrons. The velocity of the hydrogen ions after the jump is

approximately $\sqrt{-2e\varphi_U/m_H}$. In the absence of the rain their density should be equal to the density of the photoelectrons (equation (A8)) and the currentless condition can be written as $n_{ph}\left(b=b^*,\varphi=\varphi_U\right)\sqrt{-2e\varphi_U/m_H}=j_{ph}^{esc}\left(s=s^*\right)$ with the photoelectron flux from equation (A9) mapped to the jump location. Expanding this equation in powers of the small parameter b^* with the accuracy extending to the first non-vanishing term, we obtain

$$\sqrt{m_e\pi/m_H}\left(0.5-\frac{e\varphi_U}{T}\right)=1-\frac{e\varphi_U}{T}$$

where m_e and m_H are the electron and hydrogen ion masses. This equation does not have negative solutions and, therefore, the system of equations (2)–(5) has no solutions without the polar rain.

It should be noted that for $b<0.1$ the second inequality in equation (1) can be slightly violated for electrons and oxygen ions for some plasma parameters. This violation is small and can only slightly change the potential and density distributions below the jump (Appendix A provides more details).

3.3. Is the Potential Drop Localized?

The observations presented by KM2012 cannot directly answer the question about the potential distribution along magnetic field lines as it is shown in Figure 1. To address this issue, we excluded the potential jump from the model presented by equations (2)–(5), omitting from this system equation (4), and solved equations (2), (3), and (5), that is, the quasi-neutrality conditions at $s=0$ and at the upper boundary s^* together with the currentless condition. In this case, the total potential drop as a function of Γ is the same as that presented in Figure 2, but the potential distribution along the magnetic field line, calculated in a manner similar to the model with the potential jump (see section 3.2), did not converge to the potential at the upper boundary and was about 3–5 eV depending on the input parameters for the ions, photoelectron, and polar rain fluxes. These test modeling results provide a clear demonstration that the total potential drop that is presented for the different conditions in Figure 2 is mostly localized at the altitudes that are presented in Figure 3.

Remarkably, moving the injection point for all plasma components to an altitude of 1,000 km, in the region that is still collisional for both the ions and thermal electrons only slightly changes the values for the potential jumps and their locations.

4. Discussion and Conclusion

As discussed in the introduction to this paper, KM2012 and Kitamura et al. (2015; 2017) provided a comprehensive analysis of FAST observations for the geomagnetically quiet sunlit polar cap region and found that the observed potential drop over the polar cap is smaller by a factor of 2–3 in comparison to previously published model predictions (Wilson et al., 1997; Su, Horwitz, Wilson, et al., 1998). They also found that the escaping electron number flux is negatively correlated with the upward electron number flux and with the magnitude of the potential drop, while the opposite was predicted by the models. They interpreted the experimental results as evidence that "the magnitude of the field-aligned potential drop at high altitudes is likely determined mostly by the balance between the escaping photoelectron flux and the polar wind H^+ ion flux" (Kitamura et al., 2017). Such an interpretation implies complete ionospheric control of the formation of the field-aligned potential drop and completely disregards the magnetospheric input to this process discussed in the section 3. They also noted that the impact of large polar rain fluxes on the escaping photoelectron flux will be significant (Kitamura et al., 2015). The goal of this paper is to model the currentless polar wind in the presence of large potential drop (10–30 eV) for the quiet magnetospheric conditions observed by KM2012.

In the framework of the proposed model we found a good agreement between the model results and the observations (Figures 2 and 4). As can be seen from these figures, the escaping photoelectron flux is negatively correlated with the magnitude of the potential drop. The negative correlation between the escaping and reflected photoelectron fluxes cannot be explained by this model without additional assumptions. A possible reason for this effect can be found in KM2012 and involves the production of secondary electrons by the reflected photoelectron flux.

The proposed model requires the presence of a polar rain, and so in this model the potential drop is formed not only by ionospheric sources (H^+ ions and photoelectrons) as discussed by Kitamura et al. (2012; 2015; 2017), but also by a magnetospheric component, namely, polar rain electrons (Figure 2). As shown in section 3, the quasi-neutrality condition at the upper boundary of the potential jump is achieved primarily due to the balance between hydrogen ion and polar rain electron densities. The density of the polar rain strongly affects the location of the potential jump (Figure 3) and defines the ratios of the hydrogen to photoelectron fluxes for which the quasi-neutrality condition above the jump can be satisfied (Figure 2). The calculated position of the potential jump location is expressed through the magnetic field, and the calculated distance depends on the validity of the magnetic field model for these distances.

The potential distribution along the magnetic field line has two regions (see Figure 1), with a small, gradual, potential drop of 3–5 eV and a potential jump that depends primarily on the ratio between the fluxes of photoelectrons and hydrogen ions for hydrogen fluxes large compared to those of the polar rain. For hydrogen fluxes less than or comparable to the flux of the polar rain the potential jump magnitude also depends on the polar rain.

The magnitude of the potential jump depends strongly on the energy structure of the photoelectron flux (Figure 4). For the observed range of parameters presented by KM2012, the potential drop—escaping photoelectron flux dependence—is in good agreement with observations (Figure 4) and does not depend on the polar rain or oxygen flux. However, the existence of the model solution by itself requires the presence of the polar rain. In this sense, in the framework of our kinetic model, the influence of the polar rain on the potential drop/jump formation is self-evident. As we mentioned above, the polar rain represents the magnetospheric source of the potential drop formation and works together with ionospheric sources represented in the model by hydrogen ions and photoelectrons.

Without a jump the total potential drop calculated from the currentless condition and the quasi-neutrality conditions at the injection and upper boundaries is also in agreement with the observations, but such drop cannot be reached by solving the quasi-neutrality equation along the magnetic field line starting from the lower injection boundary. This supports the assumption about the existence of the potential jump at the upper boundary at the altitudes presented by Figure 3.

As discussed by Arefiev and Breizman (2009), the interaction of hot electrons (here photoelectrons) with the rarefaction wave generated by plasmas expanding in a diverging magnetic field can result in a trapped particle population. Such an additional photoelectron population at the upper boundary was included in the model under simplifying assumptions that are discussed in Appendix A of this manuscript, and it was found that for the range of the considered plasma parameters the role of the trapped photoelectrons is small.

The model permits us to quantify what should be considered large polar rain fluxes (Kitamura et al., 2015). These are fluxes comparable to those of the escaping hydrogen, as demonstrated in section 3.1.

Depending on the hydrogen photoelectron flux ratios, hydrogen ions at altitudes above the potential jump can reach escape energies of 10–30 eV. Corresponding velocities (40–80 km/s) are in the range of the velocities observed by the POLAR mission (20–110 km/s) at the distance 8 R_E during the solar minimum, year 1996 (Su, Horwitz, Moore et al., 1998).

Density and flux calculations in the model were based on the assumption that the second derivative of the potentials in equation (1) is negative. We found that this requirement is slightly violated near the upper boundary, but this violation is small and did not affect the presented results (see Appendix A for the details).

It should be noted that in this model the currentless condition did not assume the presence of the counter streaming flux of cold electrons from the upper boundary. Currentless conditions are reached due to the balance between the escaping photoelectron and hydrogen fluxes. However, the solution of (2)–(5) requires that the polar rain electrons to be taken into account.

The potential jump and its location presented in Figures 2 and 3 for different photoelectron, hydrogen ions, and polar rain fluxes are not predicted by any of modern global polar outflow models. These models, however, simulate ion and photoelectron outflows coming from ionospheric altitudes (see, e.g., Varney et al. (2014); Glocer et al., 2017). By combining these modeling parameters with polar rain inflows, and based on the findings presented in this paper, one can find the relations that will indicate the existence or not of these kind of potential jumps and their magnitude.

The polar cap electrostatic potential jump formation could have an effect on the thermal electrons. Varney et al. (2014) and Glocer et al. (2017), for example, imposed 40- and 20-V potential drops at the upper boundary of their models and took into account an additional heating of reflected photoelectrons when calculating ionospheric electron temperatures. They both found that the additional heating has only a very slight effect on thermal electron temperature calculations.

The potential jump over the sunlit polar cap region could also influence the energy balance of the thermal electrons due to the existence of the trapped photoelectron populations with energies smaller than the potential drops in the region below the potential jump location. The production of such trapped photoelectrons is similar to the trapping of the photoelectrons in closed magnetic field configurations (see Khazanov, 2010, for the details). In order for it to occur, there must be a scattering mechanism like Coulomb collisions or wave-particle interactions. We will use the SuperThermal Electron Transport code (Khazanov et al., 2015) to consider this effect in a forthcoming publication.

As can be seen from Figures 2–4, currentless and quasi-neutrality conditions are not always satisfied for some domains of the plasma parameters that have been chosen in this manuscript. An additional analysis for such of cases is required (which is out of the scope of this paper) and will be considered in future studies.

Appendix A

A1. Phase Space Description and Particle Densities and Fluxes

Plasma component density and flux calculations are performed in E-μ phase space (PS), where E is the total energy, and μ is the particle magnetic moment (Khazanov et al., 1998; Whipple, 1977). The distance along the magnetic field line, s, is measured from the injection point of the ions and cold electrons ($s = 0$, altitude 2,400 km), and expressed with the help of the magnetic field ratio $b = B(s)/B(0)$. For the photoelectrons, injected at the altitude 1,000 km and the polar rain, measured at the same altitude, the distance to the same point s is related to b by $b' = bB(2{,}400)/B(1{,}000)$. It is assumed that the potential is a negative diminishing function along the magnetic field line, φ_L and φ_U are the potentials below and above the potential jump, respectively, and the jump position is s^*. The width of the jump along the field line is neglected. It is assumed that the particles are not reflected above the jump.

A2. Photoelectron Densities and Flux

The photoelectrons PS are presented in Figure A1. The populated domain is between the E axis and the red line; E_m and E_{min} are respectively the maximum and minimum energies of the photoelectrons. The last

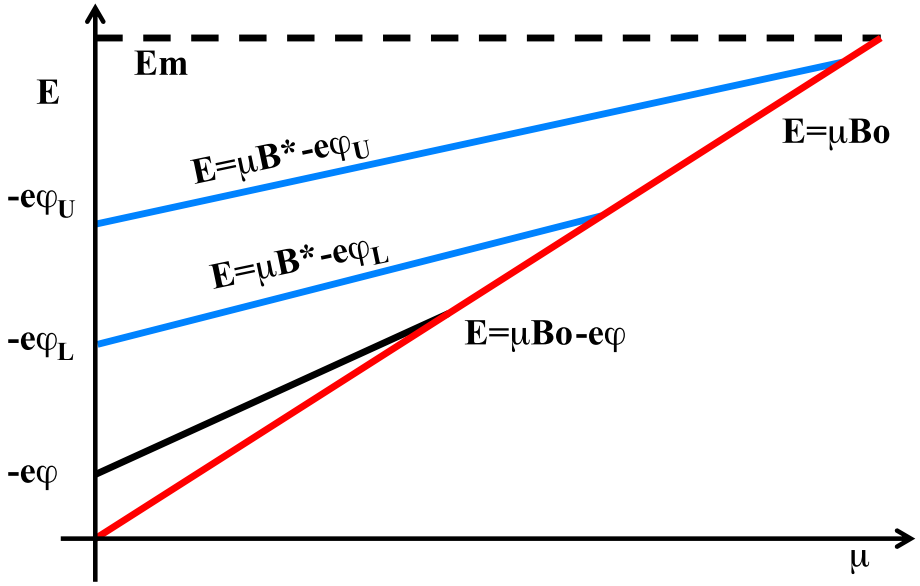

Figure A1. Phase space of the cold electrons and photoelectrons.

energy in the calculations is 0.35 eV and is not marked in the figure. Straight lines correspond to zero parallel particle velocity; they separate the particles that will be reflected below the corresponding $B(s)$ from the particles that can be found above this position. It is assumed that the black lines corresponding to different s do not intersect each other. The PS of the escaping particles is restricted by the E axis, upper blue and the red lines. To be able to overcome the potential jump$|\varphi_U - \varphi_L|$, the electrons should have energy larger than this difference when compared to the particles able to reach the position with the potential φ_L. Reflected particles at $B(s)$ are the particles able to go beyond this position excluding those that are able to escape. All particle distributions are assumed to be independent of μ.

Expressions for the electron density and flux at a point s along the magnetic field line are

$$n = \frac{\sqrt{2}\pi B(s)}{m^{3/2}} \iint \frac{f(E)}{\sqrt{E - \mu B(s) + e\varphi(s)}} \mathrm{d}E\mathrm{d}\mu \tag{A1}$$

$$j = \frac{2\pi B(s)}{m^2} \iint f(E)\mathrm{d}E\mathrm{d}\mu \tag{A2}$$

where $f(E)$ is the distribution function, m is the mass of the particle, and $\varphi(s)$ is the potential at the point s. The integration domain is defined by the portion of the PS of the injected particles that can reach the position of interest. For the injected photoelectrons, the density above the point of injection can be presented as

$$n_{ph}^{inj}(s) = \sqrt{2m}\left[\int_{-e\varphi}^{E_m} \frac{j(E)}{E}\sqrt{E + e\varphi}\mathrm{d}E - \sqrt{1-b'}\int_{E_0}^{E_m} \frac{j(E)}{E}\sqrt{E - E_0}\mathrm{d}E\right] \tag{A3}$$

where $E_0 = -e\varphi/(1 - b')$ is the energy of the point of intersection between the red and black lines, and the distribution function is expressed through the flux. If the lower limit of integration is less than $E_{\min}$ it should be changed to $E_{\min}$. For the reflected photoelectrons the following expression is found

$$n_{ph}^{rfl}(s) = n_{ph}^{inj}(s) - \sqrt{2m}\left[\int_{-e\varphi_U}^{E_m} \frac{j(E)}{E}\sqrt{E + e\varphi(s)}\mathrm{d}E - \sqrt{1-b'}\int_{E^*}^{E_m} \frac{j(E)}{E}\sqrt{E - E_0}\mathrm{d}E\right. \tag{A4}$$

$$\left. - \sqrt{\frac{b}{b^*} - 1}\int_{-e\varphi_U}^{E^*} \frac{j(E)}{E}\sqrt{E_1 - E}\mathrm{d}E\right]$$

where the energy at the point of intersection of the upper blue and the red lines is $E^* = -\frac{e\varphi_U}{1-b^*}$ with $b^* = B(s^*)/B(0)$, and $E_1 = \frac{e\varphi b^* - e\varphi_U b}{b - b^*}$.

Substituting $b = 1$ and $\varphi = 0$ in equations (A3) and (A4), the density at the ion injection point can be calculated. The photoelectron densities below and above the jump can be found by setting $b = b^*$, and $\varphi = \varphi_L$ and $\varphi = \varphi_U$ in these equations, respectively.

The density of the trapped photoelectrons at the upper boundary is estimated as follows (Arefiev & Breizman, 2009). The motion of a particle with a magnetic moment μ along a field line can be considered as a motion in the field with an effective potential of $U_{eff} = \mu B - e\varphi$. Because we assume that particles above the jump are not reflected, this potential has a maximum at the upper boundary, and further out the first term diminishes (due to diminishing B), while the second term does not grow. Particles with energies slightly larger than this maximum will be reflected by the rarefaction wave above the upper boundary with smaller energy and form the trapped population. So the trapped particles are the injected particles with $\mu = E/B_0$, and they fill the PS domain between the red line and the continuation of the upper blue line. More details of the calculation of n_{ph}^{tr} can be found in the paper by Arefiev and Breizman (2009). The density of the trapped particles is

$$n_{ph}^{tr} = 2\sqrt{2m}b^{*\prime}\sqrt{1-b^{*\prime}}\int_{E^*}^{E_m} \frac{j(E)}{E}\sqrt{E - E^*}\mathrm{d}E \tag{A5}$$

The escaping photoelectron flux at $s = 0$ is calculated from equation (A2) with integration over the PS domain of the escaping particles

$$j_{ph}^{esc}(s=0) = \frac{1}{b^*}\int_{-e\varphi_U}^{E^*} j(E)\left(1+\frac{e\varphi_U}{E}\right)dE + \int_{E^*}^{E_m} j(E)\left[1+\frac{e\varphi_U}{E}\right]dE \tag{A6}$$

A3. Cold Electron Densities and Flux

The PS of the cold electrons is the same as that in Figure A1, except that $E_m \to \infty$. For cold electrons with a Maxwellian distribution

$$f = 2n_{0c}\left(\frac{m}{2\pi T}\right)^{3/2}\exp\left(-\frac{E}{T}\right)$$

(n_{0c} is the density of the injected particles) from equation (A1) or equations (A3) and (A4), it follows that the expression for the total cold electron density

$$\begin{aligned} n_c(s) = \; & n_{0c}\left\{-\sqrt{\frac{b}{b^*}-1}e^{\frac{-E_1}{T}}\left[erfi\left(\sqrt{\frac{(e\varphi_U+E_1)}{T}}\right)-erfi\left(\sqrt{\frac{(E_1-E^*)}{T}}\right)\right]\right. \\ & \left. + \; e^{e\varphi/T}\left[1+\mathrm{erf}\left(\sqrt{e(\varphi-\varphi_U)/T}\right)\right]-\sqrt{1-b}\,e^{-E_0/T}\left(1+\mathrm{erf}\left(\sqrt{\frac{(E^*-E_0)}{T}}\right)\right)\right\} \end{aligned} \tag{A7}$$

Here $erfi(z)$ is the imaginary error function and $\mathrm{erf}(x) = \frac{2}{\sqrt{\pi}}\int_0^x e^{-t^2}dt$. For $s = 0$ the term with $\sqrt{1-b}$ vanishes and $\varphi = 0$; for the density below the jump $b = b^*$, $\varphi = \varphi_L$, and the term with the first square brackets vanishes; above the jump the reflected particles vanish and the density is

$$n_c(b=b^*, \varphi=\varphi_U) = n_{0c}\left[e^{e\varphi_U/T}-\sqrt{1-b^*}e^{-E^*/T}\right] \tag{A8}$$

The escaping flux of the cold electrons can be found substituting the distribution of the cold electrons in the expression for the flux presented above (see (A2))

$$j_c^{esc}(s=0) = \frac{n_{0c}(s=0)}{b^*}\sqrt{\frac{2T}{\pi m}}\left[e^{e\varphi_U/T}-(1-b^*)e^{-E^*/T}\right] \tag{A9}$$

A4. Polar Rain Densities and Flux

The distribution function for the polar rain injected at the upper side of the jump is taken as

$$f = 2n_{Upr}\left(\frac{m}{2\pi T}\right)^{3/2}\exp\left(-\frac{E+e\varphi_U}{T}\right)$$

where n_{Upr} is the density of downward injected particles. The PS of these electrons (Figure A2) is filled above the upper blue line. Particles from the part of the PS between the E axis, upper blue line, and the black line above their intersection are the particles able to reach the position, where the potential is $\varphi(s)$. The part of this PS domain restricted by the E axis and the red line belongs to the particles able to go below $s = 0$, that is, escaping particles. Particles reflected below the position with potential $\varphi(s)$ are the particles of the PS above the upper blue line between the black and red lines. It is assumed that when $-e\varphi$ diminishes the intersection point 2 moves toward point 1. The calculated polar rain electron density can be expressed as

$$\begin{aligned} n_{pr}(s) = \; & n_{Upr}\left\{erfcx\left(\sqrt{e(\varphi-\varphi_U)/T}\right)+\sqrt{1-b'}e^{-E^*b'^*/T}erfcx\left(\sqrt{\frac{(E^*-E_0)}{T}}\right)\right. \\ & \left. + \; \frac{2}{\sqrt{\pi}}\sqrt{\frac{b}{b^*}-1}\left[dawson\left(\sqrt{\frac{(e\varphi_U+E_1)}{T}}\right)+e^{-E^*b'^*/T}dawson\left(\sqrt{\frac{(E_1-E^*)}{T}}\right)\right]\right\} \end{aligned} \tag{A10}$$

where $erfcx(x) = e^{x^2}(1-\mathrm{erf}(x))$ and $dawson(z) = \frac{\sqrt{\pi}}{2}e^{-z^2}erfi(z)$. For the polar rain density at $s = 0$ ($b = 1$, $\varphi = 0$) the second term and the last Dawson function vanish; below and above the jump ($b = b^*$, $\varphi = \varphi_L$, $\varphi = \varphi_U$) the term with the square brackets vanishes.

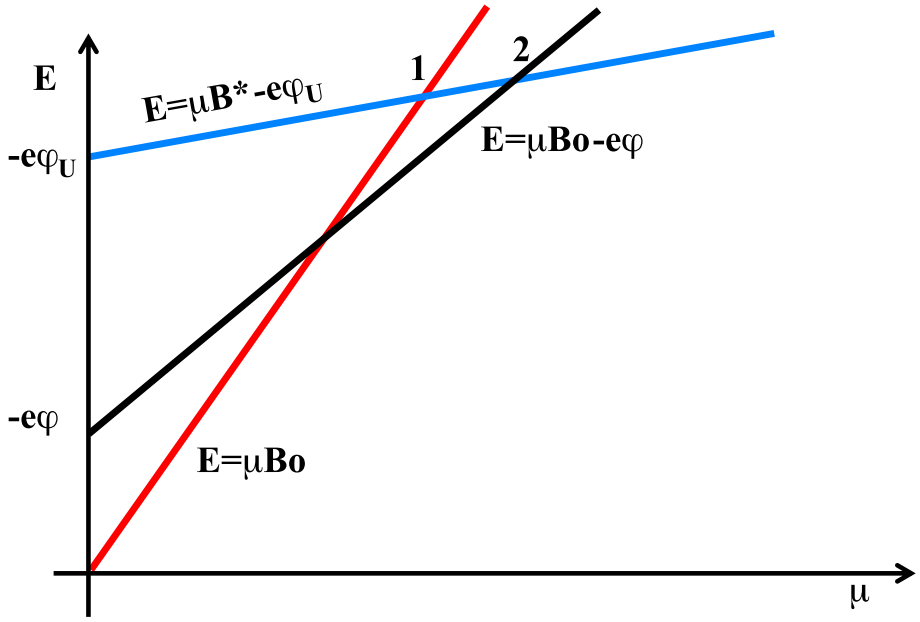

Figure A2. Phase space of the polar rain.

The escaping polar rain flux is

$$j_{pr}^{esc}(s=0)=\frac{n_{upr}}{b^{'*}}\sqrt{\frac{2T}{\pi m}}\left[1-\left(1-b^{'*}\right)e^{-E^{*}b^{'*}/T}\right] \tag{A11}$$

A5. Oxygen Ion Densities and Flux

Figure A3 presents the PS for oxygen ions. The total potential expressed with the help of the magnetic field ratio is

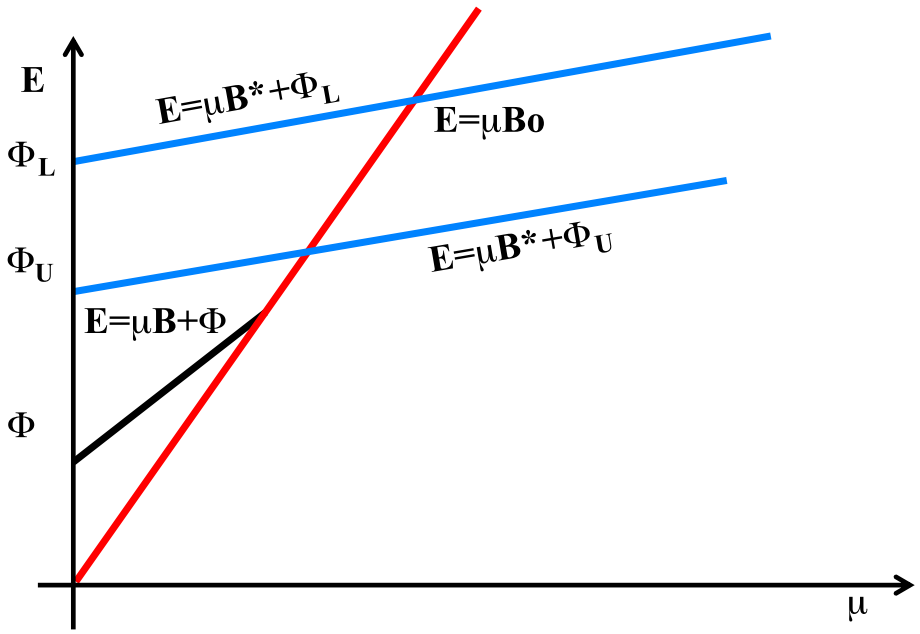

Figure A3. Phase space of the oxygen ions.

$$\Phi(s) = e\varphi + \frac{gmr_E^2}{r_0}\left(1-b^{1/3}\right)$$

where $g = 981$ cm/s^2, $r_0 = r_E + 2{,}400$ km is the position of the injection point, and r_E is the Earth radii. We expect the potential to be positive and grow until the jump and then to drop at the jump. The injected ions fill the domain of PS between the E axis and the red line. Particles above the upper blue line are able to escape; it is assumed that the black lines corresponding to different s do not intersect each other. The calculated oxygen ions density for a position s is

$$n_O(s) = n_{0O}\left\{-\sqrt{\frac{b}{b^*}-1}e^{\frac{-E_2}{T}}\left[erfi\left(\sqrt{\frac{(E_2-\Phi_L)}{T}}\right)-erfi\left(\sqrt{\left(E_2-\frac{\Phi_L}{1-b^*}\right)/T}\right)\right]\right.$$
$$\left. + e^{-\Phi/T}\left[1+\mathrm{erf}\left(\sqrt{(\Phi_L-\Phi)/T}\right)\right]-\sqrt{1-b}\;\; e^{-\frac{\Phi}{(1-b)T}}\left[1+\mathrm{erf}\left(\sqrt{\left(\frac{\Phi_L}{1-b^*}-\frac{\Phi}{1-b}\right)/T}\right)\right]\right\} \quad \text{(A12)}$$

where n_{0O} is the oxygen density at $s = 0$, Φ_L is the total potential calculated below the jump at $b = b^*$, and $E_2 = \frac{\Phi_L b-\Phi b^*}{b-b^*}$. For $s = 0$ ($b = 1$, $\Phi = 0$) the last term with the square brackets and the second term in the first square brackets vanish; on the lower boundary of the jump, $s = s^*$ ($b = b^*$, $\Phi = \Phi_L$) and only the terms in the square brackets remain. The density at the upper side of the jump $s = s^*$ ($b = b^*$, $\Phi = \Phi_U$) cannot be calculated from equation (A12) directly, because the formula is found under an assumption of a potential growing with s. This density should be calculated by integration over PS above the upper blue line, and it can be presented as

$$n_O\left(s = s^*, \Phi = \Phi_U\right) = n_O\left[e^{-\Phi_U/T}\,\mathrm{erfc}\left(\sqrt{(\Phi_L-\Phi_U)/T}\right)-\sqrt{1-b^*}\;\; e^{-\frac{\Phi_U}{(1-b^*)T}}\,\mathrm{erfc}\left(\sqrt{\frac{\Phi_L-\Phi_U}{(1-b^*)T}}\right)\right] \quad \text{(A13)}$$

The escaping oxygen flux is

$$j_O^{esc}(s=0) = \frac{n_{0O}}{b^*}\sqrt{\frac{2T}{\pi m}}\left[e^{-\Phi_L/T}-\left(1-b^*\right)\;\; e^{-\frac{\Phi_L}{(1-b^*)T}}\right] \quad \text{(A14)}$$

A6. Hydrogen Ions Densities and Flux

It is assumed that the total potential of the hydrogen ions is dominated by the polarization field and is negative everywhere above the injection point. It means that the PS of injected particles is the same as in Figure A3, that is, restricted by the E axis and the red line, but the black line will move to larger negative potentials for larger s. All injected particles are able to escape, and the domain of integration is the total PS filled by the injection. With the prescribed injected hydrogen flux, taken as a fraction of the injected photoelectron flux, the hydrogen ions flux and density, n_{0H}, at $s = 0$ are known. The density of the hydrogen ions for an arbitrary s is

$$n_H(s) = n_{0H}\left[erfcx\left(\sqrt{\Phi/T}\right)-\sqrt{1-b}\,erfcx\left(\sqrt{\frac{\Phi}{(1-b)T}}\right)\right] \quad \text{(A15)}$$

and the densities at $b = b^*$, below and above the jump, can be found from (A13), setting Φ equal to Φ_L and Φ_U, respectively. Φ here is taken for the hydrogen ions.

A7. Validity of the Model

Calculating the polar rain densities (Figure A2), we required that when $-e\varphi$ diminishes the intersection point 2 moves to point 1. This means that the domain of integration (E axis, blue line-black line) is filled by particles and does not include portions of the PS from which the injected particles were reflected closer to the injection point. A similar restriction is imposed on the particles injected from below and states that the black lines in Figures A1 and A3 should not intersect each other. This condition can be formulated as $E_0(s) < E_0(s')$, where $s < s'$, and it is less restrictive than the second inequality in equation (1). In the

range of the studied plasma parameters the restriction on the polar rain is always satisfied. For the photoelectrons, cold electrons, and oxygen ions for small b ($b < 0.1$, where the oxygen content is small) the restriction is slightly violated, but the deviation is small, $\frac{|E_0|}{E_0} < 5\%$, and will only slightly affect the cold electrons and oxygen density distributions and the potential distribution below the jump.

Acknowledgments
This work was supported by NASA grant NNH14ZDA001N-HSR MAG14_2-0062, NASA Heliophysics Internal Scientist Funding Models (HISFM18-0006 and HISFM18-0009), NASA Van Allen Probes Project, and NASA LWS Program. The data for this paper are available at the website (http://doi.org/10.5281/zenodo.1206051).

References

Abe, T., Whalen, B. A., Yau, A. W., Horita, R. E., Watanabe, S., & Sagawa, E. (1993). EXOS D (Akebono) suprathermal mass spectrometer observations of the polar wind. *Journal of Geophysical Research*, *98*(A7), 11191. https://doi.org/10.1029/92JA01971

Arefiev, A. V., & Breizman, B. N. (2009). Collisionless plasma expansion into vacuum: Two new twists on an old problem. *Physics of Plasma*, *16*(5). https://doi.org/10.1063/1.3118625

Axford, W. I. (1968). The polar wind and the terrestrial helium budget. *Journal of Geophysical Research*, *73*(21), 6855–6859. https://doi.org/10.1029/JA073i021p06855

Brambles, O. J., Lotko, W., Zhang, B., Wiltberger, M., Lyon, J., & Strangeway, R. J. (2011). Magnetosphere sawtooth oscillations induced by ionospheric outflow. *Science*, *332*(6034), 1183–1186. https://doi.org/10.1126/science.1202869

Chiu, Y. T., & Schulz, M. (1978). Self-consistent particle and parallel electrostatic field distributions in the magnetospheric–ionospheric auroral region. *Journal of Geophysical Research*, *83*(A2), 629–642. https://doi.org/10.1029/JA083iA02p00629

Glocer, A., Khazanov, G. V., & Liemohn, M. (2017). Photoelectrons in the quiet polar wind. *Journal of Geophysical Research: Space Physics*, *122*, 6708–6726. https://doi.org/10.1002/2017ja024177

Guglielmi, A., Kangas, J., Mursula, K., Pikkarainen, T., Pokhotelov, O., & Potapov, A. (1996). Pc 1 induced electromagnetic lift of background plasma in the magnetosphere. *Journal of Geophysical Research*, *101*(A10), 21493–21500. https://doi.org/10.1029/96JA01750

Gussenhoven, M. S., Hardy, D. A., Heinemann, N., & Burkhardt, R. K. (1984). Morphology of the polar rain. *Journal of Geophysical Research*, *89*(A11), 9785. https://doi.org/10.1029/JA089iA11p09785

Horwitz, J. L., Pollock, C. J., Moore, T. E., Peterson, W. K., Burch, J. L., Winningham, J. D., et al. (1992). The polar cap environment of outflowing O^+. *Journal of Geophysical Research*, *9*(7), 8361–8379.

Khazanov, G. V. (2010). *Kinetic theory of inner magnetospheric plasma, Astrophys. Space Sci. Lib.*, (Vol. 372, p. 584). New York: Springer.

Khazanov, G. V., Liemohn, M., Krivorutsky, E., & Moore, T. (1998). Generalized kinetic description of a plasma in an arbitrary field-aligned potential energy structure. *Journal of Geophysical Research*, *103*, 6871–6889. https://doi.org/10.1029/97JA03436

Khazanov, G. V., Liemohn, M. W., & Moore, T. E. (1997). Photoelectron effects on the self-consistent potential in the collisionless polar wind. *Journal of Geophysical Research*, *102*(A4), 7509–7521. https://doi.org/10.1029/96JA03343

Khazanov, G. V., Tripathi, A. K., Sibeck, D., Himwich, E., Glocer, A., & Singhal, R. P. (2015). Electron distribution function formation in regions of diffuse aurora. *Journal of Geophysical Research: Space Physics*, *120*, 9891–9915. https://doi.org/10.1002/2015JA021728

Kitamura, N., Seki, K., Nishimura, Y., Abe, T., Yamada, M., Watanabe, S., et al. (2017). In C. R. Chappell, R. W. Schunk, P. M. Banks, J. L. Burch, & R. M. Thorne (Eds.), *Thermal and low-energy ion outflows in and through the polar cap: The polar wind and the low-energy component of the cleft ion fountain. Magnetosphere-ionosphere coupling in the solar system, Geophysical Monograph 222*, (First ed.). American Geophysical Union. Published 2017 by John Wiley & Sons, Inc.

Kitamura, N., Seki, K., Nishimura, Y., & McFadden, J. P. (2015). Limited impact of escaping photoelectrons on the terrestrial polar wind flux in the polar cap. *Geophysical Research Letters*, *42*, 3106–3113. https://doi.org/10.1002/2015GL063452

Kitamura, N., Seki, K., Nishimura, Y., Terada, N., Ono, T., Hori, T., & Strangeway, R. J. (2012). Photoelectron flows in the polar wind during geomagnetically quiet periods. *Journal of Geophysical Research*, *117*, A07214. https://doi.org/10.1029/2011JA017459

Lemaire, J., Peterson, W., Chang, T., Schunk, R., Barakat, A., Demars, H., & Khazanov, G. (2007). History of kinetic polar wind models and early observations. *Journal of Atmospheric and Solar-Terrestrial Physics*, *69*(16), 1901–1935. https://doi.org/10.1016/j.jastp.2007.08.011

Lemaire, J., & Scherer, M. (1972). Ion-exosphere with asymmetric velocity distribution. *Physics of Fluids*, *15*(5), 760–766. https://doi.org/10.1063/1.1693981

Lie-Svendsen, O., & Rees, M. H. (1996). An improved kinetic model for the polar outflow of a minor ion. *Journal of Geophysical Research*, *101*(A2), 2415–2433. https://doi.org/10.1029/95JA02690

Newell, P. T., Liou, K., & Wilson, G. R. (2009). Polar cap particle precipitation and aurora: Review and commentary. *Journal of Atmospheric and Solar-Terrestrial Physics*, *71*(2), 199–215. https://doi.org/10.1016/j.jastp.2008.11.004

Pollock, C. J., Chappell, C. R., Horwitz, J. L., & Winningham, J. D. (1991). Two-spacecraft charged particle observation interpreted in terms of electrostatic potential drops along polar cap field lines. In G. R. Wilson (Ed.), *Modeling magnetospheric plasma processes*, *Geophys. Mono. # 62*, (pp. 111–118). Washington D, C: AGU.

Schunk, R. W., & Nagy, A. F. (2009). *Ionospheres*, (2nd ed.). Cambridge, U. K: Cambridge Univ. Press.

Su, Y.-J., Horwitz, J. L., Moore, T. E., Giles, B. L., Chandler, M. O., Craven, P. D., et al. (1998). Polar wind survey with the Thermal Ion Dynamics Experiment/Plasma Source Instrument suite aboard POLAR. *Journal of Geophysical Research*, *103*, 29,305–29,337.

Su, Y. J., Horwitz, J. L., Wilson, G. R., Richards, P. G., Brown, D. G., & Ho, C. W. (1998). Self-consistent simulation of the photoelectrondriven polar wind from 120 km to 9 R_E altitude. *Journal of Geophysical Research*, *103*(A2), 2279–2296. https://doi.org/10.1029/97JA03085

Tam, S. W. Y., Yasseen, F., Chang, T., & Ganguli, S. B. (1995). Self-consistent kinetic photoelectron effects on the polar wind. *Geophysical Research Letters*, *22*(16), 2107–2110. https://doi.org/10.1029/95GL01846

Varney, R. H., Solomon, S. C., & Nicolls, M. J. (2014). Heating of the sunlit polar cap ionosphere by reflected photoelectrons. *Journal of Geophysical Research: Space Physics*, *119*, 8660–8684. https://doi.org/10.1002/2013JA019378

Whipple, E. C. (1977). The signature of parallel electric fields in a collisionless plasma. *Journal of Geophysical Research*, *82*(10), 1525–1531. https://doi.org/10.1029/JA082i010p01525

Wilson, G. R., Khazanov, G. V., & Horwitz, J. L. (1997). Achieving zero current for polar wind outflow on open flux tubes subjected to large photoelectron fluxes. *Geophysical Research Letters*, *24*(10), 1183–1186. https://doi.org/10.1029/97GL00923

Wiltberger, M., Lotko, W., Lyon, J. G., Damiano, P., & Merkin, V. (2010). Influence of cusp O^+ outflow on magnetotail dynamics in a multifluid MHD model of the magnetosphere. *Journal of Geophysical Research*, *115*, A00J05. https://doi.org/10.1029/2010JA015579

Winglee, R. M., Chua, D., Brittnacher, B., & Parks, G. K. (2002). Global impact of ionospheric outflows on the dynamics of the magnetosphere and cross-polar potential. *Journal of Geophysical Research*, *107*(A9), 1237. https://doi.org/10.1029/2001JA000214

Winningham, J. D., & Gurgiolo, C. (1982). DE-2 photoelectron measurements consistent with a large scale parallel electric field over the polar cap. *Geophysical Research Letters*, *9*(9), 977–979. https://doi.org/10.1029/GL009i009p00977

Yau, A. W., Abe, T., & Peterson, W. K. (2007). The polar wind: Recent observation. *Journal of Atmospheric and Solar-Terrestrial Physics*, *69*(16), 1936–1983. https://doi.org/10.1016/j.jastp.2007.08.010

Yau, A. W., Whalen, B. A., Abe, T., Mukai, T., Oyama, K. I., & Chang, T. (1995). Akebono observations of electron temperature anisotropy in the polar wind. *Journal of Geophysical Research*, *100*(A9), 17451. https://doi.org/10.1029/95JA00855